

Article

Experimental and FEM Studies of Continuous Drive Friction Welding of Ferritic Spheroidal Graphite Cast Iron

Radosław Winiczenko ^{1,*} and Andrzej Skibicki ²

¹ Institute of Mechanical Engineering, Warsaw University of Life Sciences, Nowoursynowska 166, 02-787 Warsaw, Poland

² Faculty of Mechanical Engineering, Bydgoszcz University of Science and Technology, Kaliskiego 7, 85-789 Bydgoszcz, Poland; andrzej.skibicki@pbs.edu.pl

* Correspondence: radoslaw_winiczenko@sggw.edu.pl

Abstract: Experimental and FEM studies of the friction welding process of spheroidal graphite cast iron (SGCI) are presented. A coupled thermal and mechanical 2.5 D FEM model was used to simulate the continuous drive friction welding (CDFW) process. The FE model predicted the peak temperature of the joint, effective stress, axial shortening, and the weld flash size. Additionally, the friction force on the axial shortening of specimens was studied. The peak temperatures were measured both on the axis and at the surface of the specimen. The predicted maximum temperatures in the axis, 1/2 radius, and 2 mm from the surface of the sample amounted to 1162 °C, 1177 °C, and 1061 °C, respectively. The maximum temperature of the spheroidal graphite cast iron joint was below the melting temperature of the base material (~1350 °C). The predicted temperature curves, outbursts, and shortening of welded elements indicated a good match with real models.

Keywords: spheroidal graphite cast iron; friction welding; FEM



Citation: Winiczenko, R.; Skibicki, A. Experimental and FEM Studies of Continuous Drive Friction Welding of Ferritic Spheroidal Graphite Cast Iron. *Processes* **2024**, *12*, 719. <https://doi.org/10.3390/pr12040719>

Academic Editors: Qian Zhi and Rogante Massimo

Received: 11 February 2024

Revised: 9 March 2024

Accepted: 28 March 2024

Published: 2 April 2024



Copyright: © 2024 by the authors. Licensee MDPI, Basel, Switzerland. This article is an open access article distributed under the terms and conditions of the Creative Commons Attribution (CC BY) license (<https://creativecommons.org/licenses/by/4.0/>).

1. Introduction

Rotary friction welding (FRW) is an effective welding method using the heat of friction without melting the joined material [1,2]. The heat required to weld two samples is a result of the conversion of mechanical energy into thermal energy. The friction process takes place when an axial force is used on the rotating part. After the friction process is completed, the spindle is stopped, and the upsetting force is applied. At this moment, the process of plastic deformation of the joined materials takes place. The final effect of this process is the axial shortening (upset) of the elements and the appearance of a weld flash [3]. The heat expanded at the interface quickly raises the temperature of the samples, over a very short axial distance. Welding appears under the effect of pressure that is applied while the heated zone is in the plastic temperature range.

Due to the complexity of the friction welding process, the impact of thermal and mechanical phenomena must be considered on the quality of the joint. Similar to metal forming processes, friction welding leads to a change in geometry and boundary conditions associated with heat-transfer problems. Moreover, many physical phenomena as well as plastic deformation, friction heat deformation, and stress accompanied the friction welding process. The high-temperature gradients and extensive deformation occur in the rubbing surface and the heat-affected zone. The heat-affected zone (HAZ) experiences and temperature changes are subject to several microstructural transformations during the welding process. Also, the severe local thermal excursion plays a pivotal role in determining the residual stresses in the rotary friction welding joint. Therefore, the modelling of the thermal evolution field is an important objective for the friction welding method [4]. The friction welding process is very complex in practice. Therefore, it was necessary to develop simple analytical solutions for the heat flow of the FRW welding process by many authors [5–7]. The heat flux distribution and thermal curves in the welds were determined [8,9].

The authors of works [10–12] studied the thermal processes of friction welding using analytical methods such as the finite difference method (FDM) and the finite element method (FEM). The numerical analysis of friction welding using the above methods was studied [13,14]. A coupled thermo-mechanical model in steel was proposed by the author [15]. A model predicted the heat flux, axial shortening, and flash deformation in the weld. Also, the FDM was applied to similar aluminium-aluminium and dissimilar aluminium steel bars [16]. The coupled thermo-mechanical problem also was presented [17]. The effective stress, strain rate heat, and plastic flow during the upsetting stage of the welding process were studied [18]. The new thermal law for the simulation of the CDFW process was developed [19]. Further works are related to the research study of dissimilar materials using the inertia friction welding process [15,20]. The FEM study of the diffusion phenomena in friction welding of aluminium to ceramics was reported [21]. Temperature field, residual stress, and heat flux distribution during the welding of carbon steel were investigated [22]. Modelling of the diffusion phenomena between aluminium and ceramic joints was a concern in the work [23].

Ductile cast iron is a casting material with good castability and machinability. Compared to other cast irons, ductile cast iron has better mechanical properties such as tensile strength, good plastic properties, and impact strength. The elongation for these cast irons can be up to about 22%. The tensile strength of cast iron with spheroidal graphite can range from 900 MPa to 1.7 GPa for Austempered Ductile Iron (ADI) cast iron. SGCI has a good vibration damping ability and resistance to corrosion in many aggressive media. Additionally, ductile cast iron is characterized by high abrasion resistance. SGCI has a higher strength-to-weight ratio, lower damping capacity, better machinability, and better castability compared to cast steel. Hence, spheroidal graphite cast iron is used to replace many more expensive parts made in cast steel. Elements made of cast iron are turbochargers, gearboxes and gears, steering gear, pump components, and shafts and spindles. Spheroidal graphite cast iron is a material which is difficult to weld because of its highly heterogeneous microstructure consisting of nodular graphite in a matrix of alloyed pearlite and/or ferrite. The difficulties result from the brittleness of cast iron and its high tendency to crack. The high expansion coefficients of cast iron lead to high stresses in the welded material. This often results in hard white cast iron in the weld. According to many research papers, the graphite in cast iron acts as a lubricant that prevents the production of the appropriate amount of heat, which is necessary to produce a good joint. During the welding of ductile cast iron, the spheroidal graphite is deformed, creating an unfavourable structure. A big problem in the process of joining ductile cast iron is ensuring the optimal temperature. It is difficult to determine in the joint plane under rapidly changing process conditions. Additionally, difficulties arise from determining the conditions and coefficients such as the friction coefficient, thermal conductivity, and unit pressures that change with increasing temperature.

Many works [24–26] are devoted to the difficulties when welding SGCI. The microstructures, mechanical features, and temperature estimation in spheroidal cast iron friction-welded joints were investigated in paper [24]. The microstructural features and influence of welding parameters on the tensile strength of dissimilar low-carbon steel and ductile iron joints were reported in references [25,26]. Recently, cast iron and phosphor bronze friction-welded joints with acceptable mechanical and metallurgical properties were obtained in work [27]. The effects of friction welding conditions on the tensile strength of ductile cast iron and 5052 aluminium alloy joints were also investigated [28].

Modern modelling methods allow the thermal cycle of the welding process to be determined with high accuracy. FEM methods explain thermal phenomena and their relationship with the welding parameters. The use of numerical methods, in addition to cognitive features, significantly reduces research costs and time for laboratory experiments. Recently, many interesting solutions have been achieved in welding using modern numerical techniques. A novel modelling approach for multi-pass butt-welded plates was proposed [29]. In a paper [30], the authors used artificial neural networks in nonlinear numerical simulation for estimating the thermal profile in arc welding. Experimental

analysis and numerical simulation of laser welding of thin austenitic stainless-steel sheets were conducted in paper [31].

Determining the maximum temperature and its course over time as well as the cooling rate of the joints have an important impact on the structure of welded materials in the area of contact surfaces. In the above literature, there are no reports regarding the variation of heat transfer and plastic deformation with various welding parameters of ductile cast iron joints. The welding of the SGCI bar using the CDFW process was not simulated using the SFTC DEFORM ver.11.0 commercial software.

This study aims to develop an FEM model to simulate nonlinear thermo-mechanical phenomena in the CDFW process of ductile cast iron. Determining temperatures, stresses in the welding plane, and plastic deformation will allow for accurate control of the welding process of SGCI. The predicted temperature fields, flash morphologies, and axial shortening of the models were compared with experimental data.

2. Methodology

2.1. Materials

Spheroidal graphite cast iron (SGCI) 400-17 was used for the CDFW process. The alloying elements of SGCI are presented in Table 1.

Table 1. Spheroidal of ductile cast iron elements (wt.%) and mechanical properties.

SGCI	C	Si	Mn	P	S	Mg	Fe Rest
	3.42	2.86	0.49	0.030	0.050	0.025	
Tensile Strength (MPa)	Yield Strength (MPa)		Elongation (%)		Hardness (HB)		
441	316		22		165		

2.2. Experimental Procedure

The cylindrical samples with a length of 100 mm and a diameter of 20 mm were prepared for the welding process. A similar experimental procedure was conducted in papers [24–26]. The joining of cast iron samples was performed on a friction welder with a continuous drive (ZT4-13 type) in Bydgoszcz (Poland). Figure 1 shows the experimental setup of thermocouples (TP203K1 type) for welding. The thermocouples with a diameter of approximately 1.2 mm were used for temperature measurement (Figure 1a). Figure 1b shows a diagram of the arrangement of thermocouples in a non-rotating specimen. The positions (1, 2, 3) of measurement were placed at a distance of 2, 4, and 6 mm from the bondline. The temperature measurement during the friction welding process of the two samples was recorded using a UT325 contact-type thermometer.

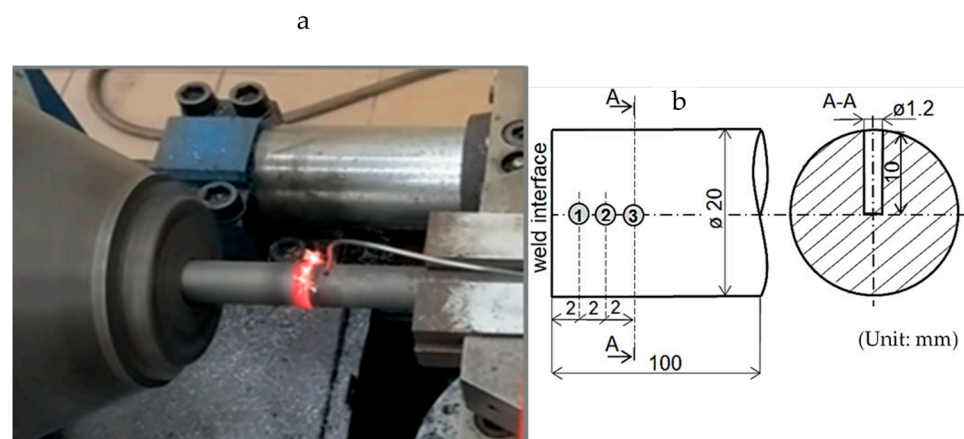


Figure 1. The experimental setup of thermocouples (a) and scheme of measurements (b) during friction welding of spheroidal graphite cast iron.

2.3. Numerical Procedure

A finite element modelling SFTC software, 'DEFORM 2.5D' ver.11.0, has been applied to the study. The software is especially capable of solving problems involving a large plastic deformation via remeshing. Figure 2 shows the geometry with a mesh of the model.

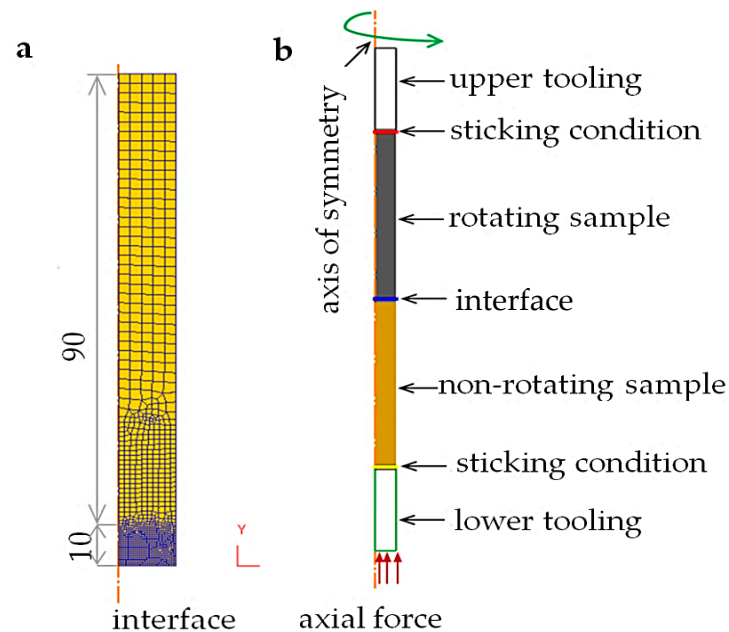


Figure 2. The mesh of the samples of the axisymmetric model (a) and sticking condition (b).

A 2.5 D analysis of one-half of the specimen was employed because of the axisymmetric shape of the specimen (Figure 2a). The circumferential impact was considered in the simulation. The mesh contained 1063 elements and 1160 nodes. The dimensions in the model were consistent with the experiment. The different mesh-size windows were applied. A mesh size of 0.03 mm was used in the region containing the weld interface. Preliminary results show that, as the mesh size is reduced at the interface, the total axial shortening (upset) predicted by the model converges on a value (11.6 mm). This occurs at a mesh size of 0.03 mm, which is suggested to be a mesh size appropriate to the modelling of the friction welding process [32]. Further away from the joint, a mesh size of 0.1 mm was used across the model. A small mesh size was applied in the interface to improve the accuracy of the numeric simulation. Finally, the mesh size was chosen so as not to generate long computation times. Additionally, an adaptive re-meshing algorithm was used to maintain good mesh quality. The algorithm was used to solve the excessive element distortion due to extensive plastic deformation and to ensure a successful computation. A suitable adaptive re-meshing parameter based on a preliminary study was applied for the expanded model to keep both the computational cost and accuracy of the model.

Figure 2b shows the model with the sticking conditions at the contact point. This axisymmetric model takes into account both the axial force to the lower tooling and the rotational speed for the upper tooling.

2.4. Governing Equations of the Mechanical and Thermal Effects

A coupled heat-transfer analysis and deformation are implemented in this model. In each time step, the deformation analysis is performed first to calculate the velocity field with the given temperature distribution and the friction conditions. The heat-transfer analysis is then undertaken to calculate the temperature distribution by considering heat generation from friction and plastic deformation and the heat flux at the interface. Additionally, heat loss to the environment, radiation, and conduction between and within the components are considered.

The deformation analysis leans on the minimum work rate rule, where it is assumed that during the metal forming process, the material flows into a shape that acts as the path of least resistance. The basic steps of the work rate are expressed [33] as:

$$\pi = \int_V \bar{\sigma} \dot{\bar{\epsilon}} dV - \int_{S_f} F_t u_t dS. \quad (1)$$

Equation (2) has to be satisfied to attain the minimum work rate:

$$\delta\pi = \int_V \bar{\sigma} \delta \dot{\bar{\epsilon}} dV - \int_{S_f} F_t \delta u_t dS + K \int_V \dot{\epsilon}_V \delta \dot{\epsilon}_V dV = 0 \quad (2)$$

where π is the work rate, $\bar{\sigma}$ is the effective stress (Von Mises stress), $\dot{\bar{\epsilon}}$ is the effective strain rate, $\dot{\epsilon}_V$ is the volumetric strain rate, F is the surface traction, u is the velocity, and K is a penalty constant.

The thermal estimation is executed by providing the following equation:

$$\int_V kT \delta T dV + \int_V \rho c \dot{T} \delta T dV - \int_S q_n \delta T dV - \kappa \left(\int_V \delta_{ij} \epsilon_{ij} \delta T dV + \int_S (f_s)_t (u_s)_t \delta T dS \right) = 0 \quad (3)$$

where k indicates the thermal conductivity, q_n is the heat flux across the weld interface, ρc is the heat capacity, f_s is the traction vector, u_s is the sliding velocity vector, and κ is the coefficient that is used to convert the mechanical work into heat.

2.5. Heat Input and Friction Coefficient

During sliding friction, heat generation at the contacting surfaces depends on the friction coefficient, the normal pressure, and the sliding speed. Similarly, in friction welding, heat generation at the weld interface depends on the friction coefficient between contacting substrates, the friction pressure, the rotational speed, and the rod diameter. The friction coefficient is a parameter particularly important during friction welding. The friction coefficient depends on many factors, among them the contacting materials and the environmental conditions. Therefore, in this study, the friction coefficient and surface pressures were taken into account between the welded materials. Calculating the heat generated at the weld interface during friction welding includes many problems such as the selection of the friction coefficient and the pressure distribution at the contacting interface when a rod is employed during the welding process. The heat generated per area unit during friction welding can be described as:

$$\frac{q_0}{A} = \frac{1}{A} \int_0^T \mu P V_{max} = \frac{r}{R} 2\pi r dr = \frac{2}{3} \mu P V_{max} \quad (4)$$

where q_0 is a net power, A is a cross-section, P is axial pressure, μ is the friction coefficient, and V_{max} is a velocity at the outer periphery of the test sample.

In the case of the low temperature, the friction stress is calculated using the Coulomb friction law according to the expression

$$\tau_f = -\mu \sigma_n \frac{v_s}{|v_s|} \quad (5)$$

where τ_f is the shear friction, σ_n is the normal stress, v_s is the sliding velocity, and the negative sign characterises the opposition between the friction stress. The friction coefficient μ can be estimated [14] as:

$$\mu = a \cdot P^b T^c \exp(dV) \quad (6)$$

where P , T , and V are the axial pressure, temperature, and linear velocity, and a , b , c and d are the constants obtained from the experiments.

In the case of high temperature, the shear friction law is assumed and can be presented with the formula:

$$\tau_f = -mk \frac{v_s}{|v_s|} \quad (7)$$

where k is the shear yield stress of the material, and m is the friction factor.

There are various ways of selecting the friction coefficient (μ) in the references. The μ was assumed to be constant in the simulation of CDFW [34–37]. The constant value of friction coefficient μ was established by comparing the computed and investigated data selected from the previous researchers. Additionally, the von Mises flow criterion was used to express the relationship between the shear stress and the yield flow stress for hot working at high temperatures, and the value of 0.577 was set to the constant μ in the sliding friction stage. The μ was calculated as a function of temperature by the experiment measurement [20,38]. The μ that only related to sliding velocity was also used in the numerical simulation [39]. Recently, the friction coefficient related to temperature, pressure, and sliding velocity was applied in the numerical calculation of the welding process [40–45].

As a result of repeated numerical simulations, it was established that the shear friction of 0.5 gave the close results of temperature and shortening material obtained by the experiment.

2.6. Thermophysical Properties

The thermophysical properties of SGCI are taken from the ASM handbook [4]. Moreover, specific heat and thermal conductivity for ductile iron are shown in Figure 3.

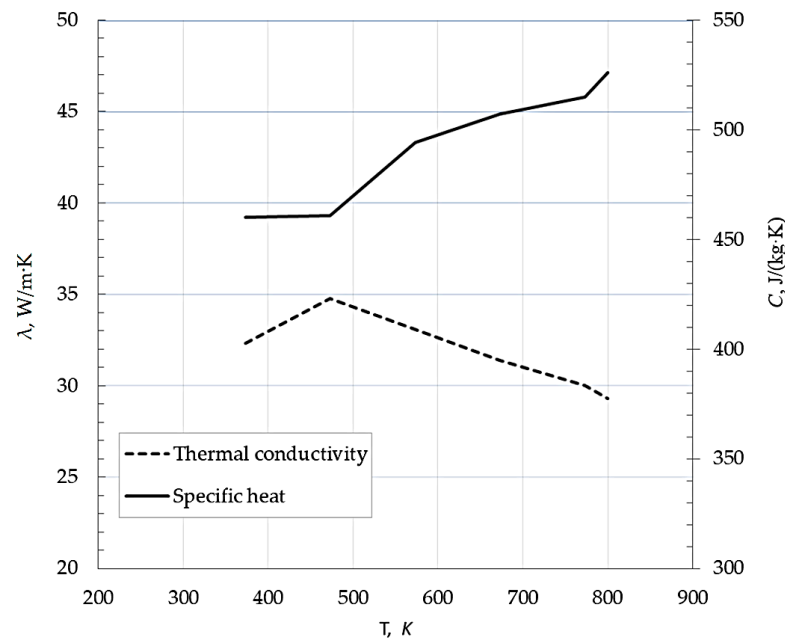


Figure 3. Thermal conductivity and specific heat of spheroidal graphite cast iron versus temperature.

Friction welding is a welding method that concerns both heating and plastic deformation of the base material under extreme thermal and strain rate conditions. During the friction stage, the material is subjected to high temperatures, initially at low strain rates. In the forging stage of the welding process, the material is subsequently brought into the fully plasticised region where the strain rate may exceed 10^3 s^{-1} .

2.7. Material Model

The Johnson–Cook (J–C) model, as the constitutive material model, was applied to simulate the friction welding process. This model refers to the strains, strain rates, flow

of stresses, and temperature distribution in the investigated object. The J–C equations are usually used for the simulation of materials subjected to deformation in a wide range of strain rates and temperatures. The J–C model takes into account the impacts of strain, strain rate hardening, and also thermal softening. Moreover, the flow stress at each simulation step can be estimated quickly [34]. The J–C model for dissimilar materials has been already employed to simulate the friction welding process [34,46,47].

The general form of the Johnson–Cook equation is expressed as:

$$\sigma = [A + B(\varepsilon)^n] [1 + C \ln(\dot{\varepsilon})] [1 - (T^*)^m] \quad (8)$$

where σ is the effective flow stress; the A , B , C , m , and n are the model parameters (A is the proof stress at ambient temperature and the strain rate, B is the coefficient of strain hardening, C is the strain rate sensitivity parameter, responsible for the kinematic strengthening, m is the temperature coefficient, and n is the strain hardening exponent); ε is the effective plastic strain; and $\dot{\varepsilon} = \dot{\varepsilon} / \dot{\varepsilon}_0$ is the dimensionless strain rate, where $\dot{\varepsilon}$ is the strain rate and $\dot{\varepsilon}_0$ is the reference strain rate. T^* is the homologous temperature and is as follows:

$$T^* = \frac{T - T_{ref}}{T_m - T_{ref}} \quad (9)$$

where T is the absolute temperature, T_{ref} is the reference temperature, and T_m is the melting temperature $T > T_{ref}$ [34].

JCM parameters for spheroidal graphite cast iron are tabulated in Table 2.

Table 2. Johnson–Cook parameters for SGCI [48].

A , MPa	253.7
B , MPa	638.9
n	0.4969
C	0.26573
m	1.037
T_{room} , K	293
T_{melt} , K	1573

During the welding process, the temperature in the weld area rises sharply due to intense friction and plastic flow. To calculate the temperature distribution, the heat transfer analysis is undertaken by considering the frictional heat generation at the weld interface, heat generation by plastic deformation, and heat loss to the environment. The quality of the weld is mostly affected by the interface temperature changes in the welding process. It is important to study the optimum range of parameters and temperature profiles to obtain good welds. It is necessary to take into account not only thermo-mechanical changes on the contact surfaces of welded elements but also those caused by convection and radiation. The temperature of the environment was set to 20 °C. The convective heat transfer coefficient was assumed to be 10 W/(m²K).

3. Results and Discussion

3.1. Temperature Distribution

Temperature contours during the friction phase (a–c) and upsetting stage (d–f) of the CDFW process of the SGCI are presented in Figure 4.

As can be seen in the graphs, the friction welding process begins in the places most distant from the axis of the cylindrical samples. This is where the highest peripheral speed appears, where the material stays plasticized as a result of the growing temperature. A relatively rapid increase in temperatures during the friction period of the samples is shown in Figure 4a. After 8 s, the maximum temperature on the surface was obtained at 1200 °C. This constant high temperature remains throughout the entire friction period of welding (Figure 4b,c). Moreover, a significant flash formation appeared during the

friction stage. The temperature profiles of the weld zone during the upsetting stage are shown in Figure 4d–f. During the upsetting stage, the joint flash increases as a result of the plastic deformation.

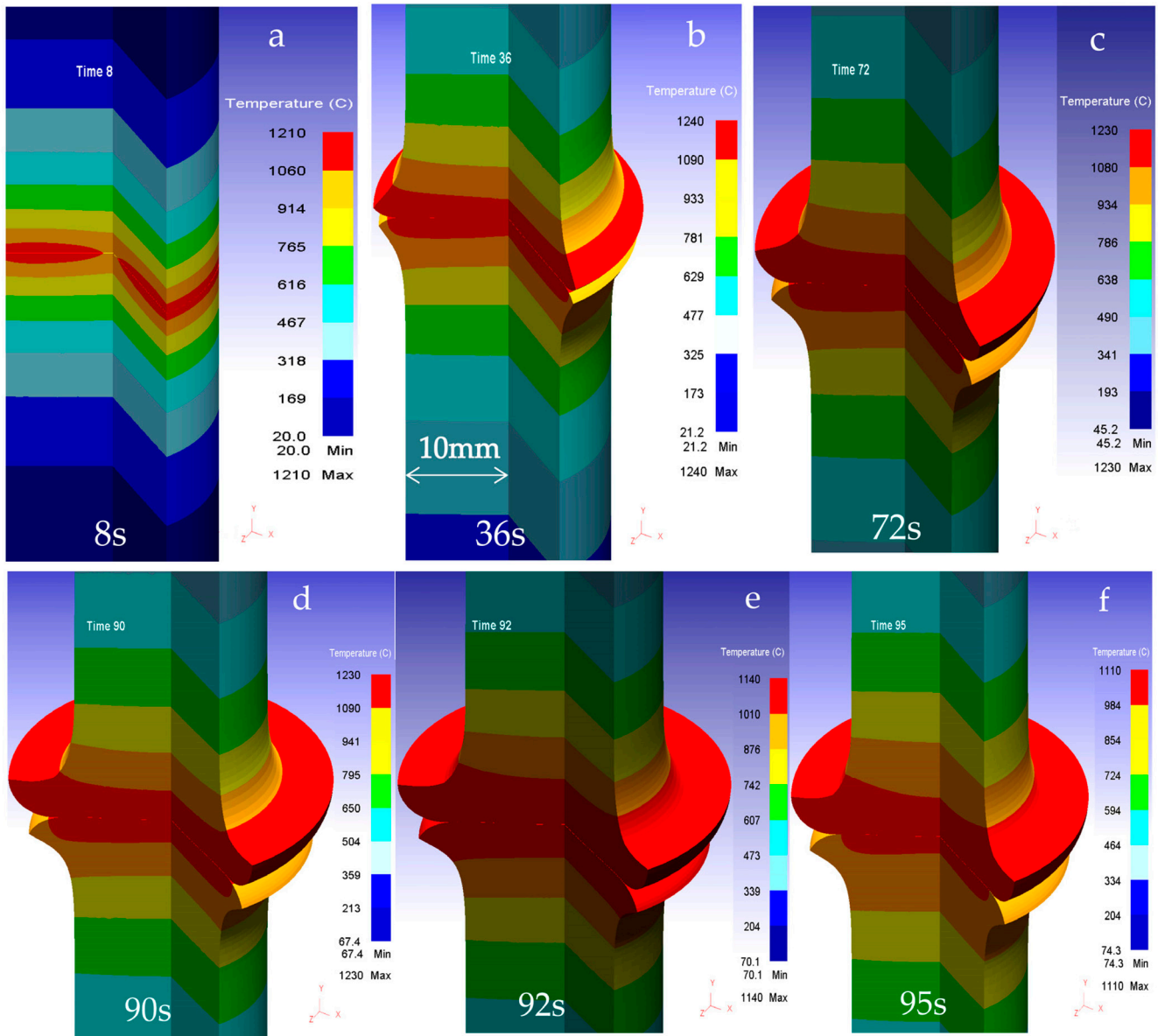


Figure 4. Temperature contours of SGCI during friction stage (a–c) and upsetting stage (d–f) for welding parameters: $P_t = 37$ kN, $P_{sp} = 33$ kN, $T_t = 90$ s, $UT = 3$ s, and $n = 1450$ rpm 4 (3D visualization of the axisymmetric model).

The maximum interface temperature of 1227 °C of the weld was attained in a friction time of 45 s (Figure 5). Moreover, a quasi-stable temperature phase with a fluctuation was visible.

It can be observed that during the upsetting stage, the temperature dropped by approximately 100 °C. A significant shortening of the cast iron can be seen, because a plastic deformation takes place (Figure 6). Figure 5 shows the maximum axial shortening of 11.62 mm is reached during the upsetting phase of the welding process. The predicted axial shortening does not differ significantly from the shortening of the welded elements (12.35 mm).

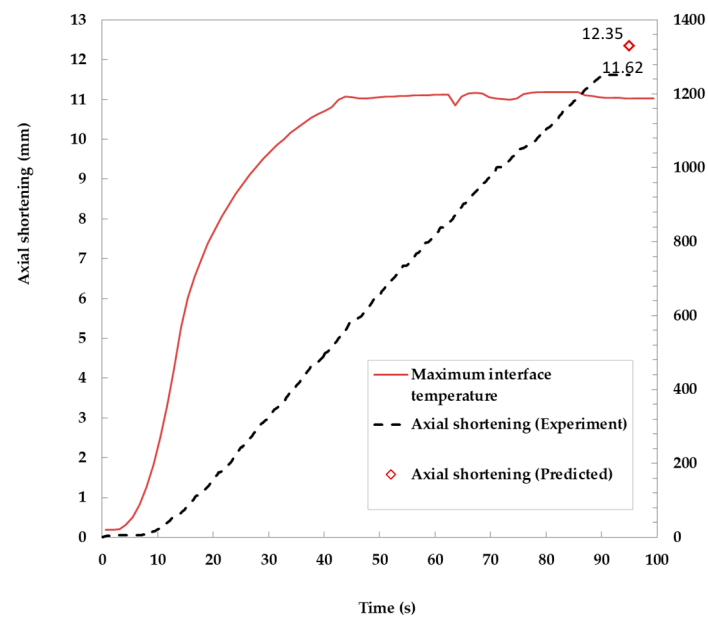


Figure 5. Axial shortening and maximum temperature profile during friction welding.

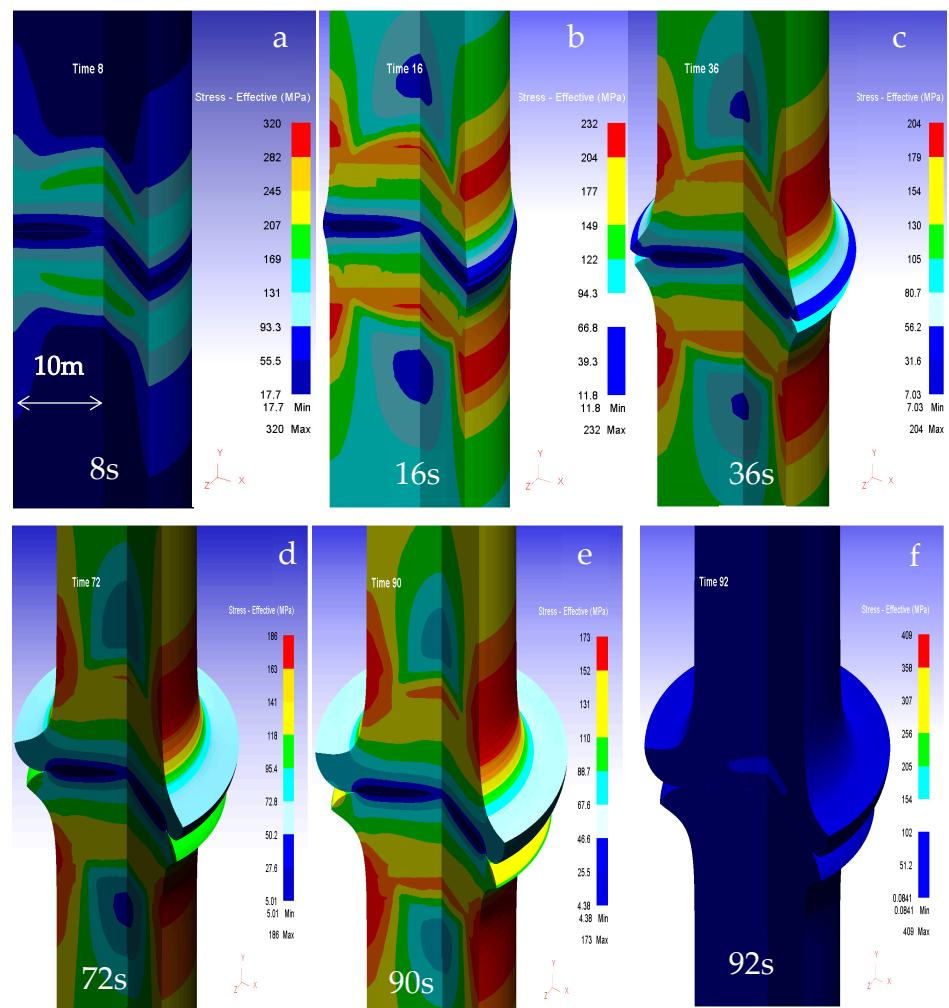


Figure 6. Effective (von Mises) stress contours of SGCI during friction stage (a–c) and upsetting stage (d–f) for welding parameters: $P_t = 37$ kN, $P_{sp} = 33$ kN, $T_t = 90$ s, $UT = 3$ s, and $n = 1450$ rpm 4 (a 3D visualization of the axisymmetric FE model).

3.2. Effective (von Mises) Stress Distribution

Figure 6 presents the stress contour during the friction stage (a–c) and upsetting stage (d–f) of the welding process.

Figure 6 shows that the effective stresses of the specimen during the friction are relatively small. The effective stress values are 93, 65, and 56 MPa for 8, 16, and 36 s friction times, respectively. At the friction stage (Figure 6d), there is a sudden increase in stress that achieves a maximum of 173 MPa on the surface of the joint. The constant effective stress value takes place during forging from 92 to 95 s (Figure 6e). The constant effective stress value occurs during the upsetting phase of the welding process from 92 to 95 s (Figure 6e). As can be seen from Figure 6f, the stresses gradually reduce and attain a value of 100 MPa. After stopping the welding process, the stresses fall to zero. Also, it can be seen that the effective stress is the lower interior of the weld interface compared to the peripheral specimen. The friction stress is proportional to the shear yield strength [15].

Figure 7 shows thermal profiles in the spheroidal cast iron for various positions from the weld interface.

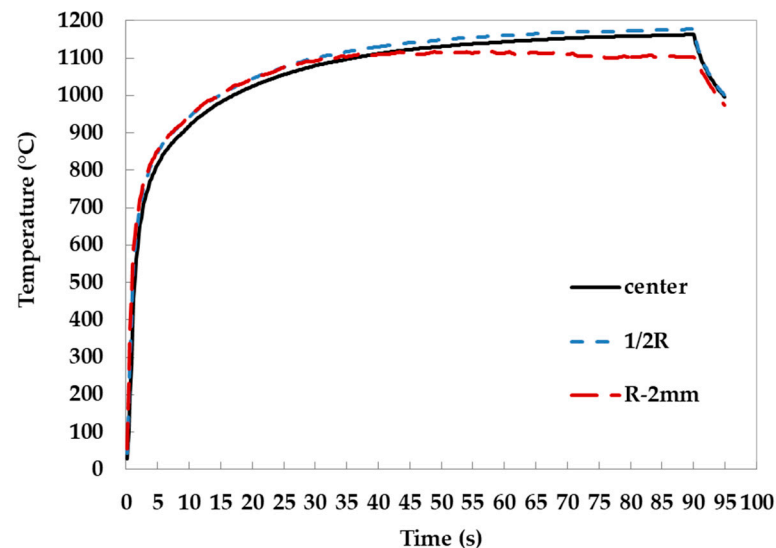


Figure 7. Thermal curves in spheroidal cast iron weld.

The nature of the temperature distribution is similar for all measurement locations. It can be seen that the temperature in $\frac{1}{2} R$ is the highest, while, in the 2 mm form, the surface has the lowest value. This indicates that heat concentrates here. The highest temperature values were obtained for the welding time of 90 s. It can be seen that the temperature rises logarithmically with growing friction time. After getting the highest value of about 1162 °C, the temperature drops fast to 985 °C during the upsetting phase of the welding process (Figure 7). The predicted maximum temperatures in the axis, $\frac{1}{2}$ radius, and 2 mm from the surface of the sample amounted to 1162 °C, 1177 °C, and 1061 °C, respectively.

3.3. Validation

3.3.1. Temperature Validation

The temperature curves in the non-rotating SGCI side are compared in Figure 8. The simulation results were attained under the friction force (FF), friction time (FT), upsetting force (UF), upsetting time (UT), and rotating speed (RS) of 24 kN, 90 s, 24 kN, 3 s, and 1450 rpm, respectively. Thin thermocouples were used to measure the temperature during welding at distances of 2, 4, and 6 mm from the initial bond line on the axis of the samples (see scheme in Figure 1b).

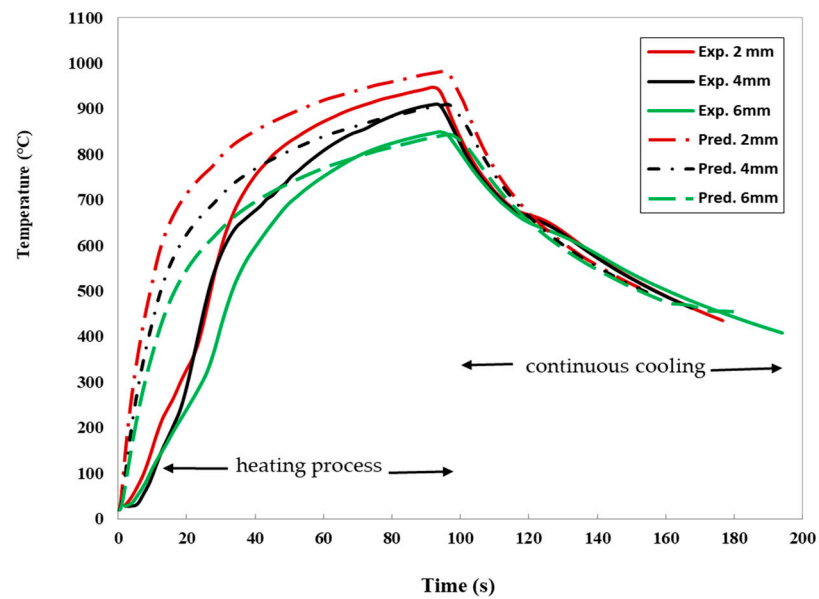


Figure 8. The experimental and predicted in non-rotating SGCI side along the axis at a distance of 2, 4, and 6 mm from the original weld interface.

Figure 8 shows that the overall tendency with the distance from the interface is well reflected by the CDFW model. The values of the modelled temperatures are slightly higher than the experimental ones in the initial phase of friction. The time constant of the thermocouples may be responsible for the discrepancy [22,49]. After 40 s, the differences were small. During the cooling process (from a time of 100 to 200 s), the measured and computed temperature profiles are almost identical (Figure 8).

3.3.2. Macroscopic Morphology Validation

The size of the flash is a significant factor related to the weld quality. The flash size is large enough that the hot plasticized material is expelled from the interface. The dimensions of the flash and welded samples are the basic parameters for assessing the quality of the joint [35,37,38]. Therefore, both 'upset' and weld flashes of the specimens have been measured. Figure 9 shows a comparison of the weld flash dimensions with a model from the numerical simulation.

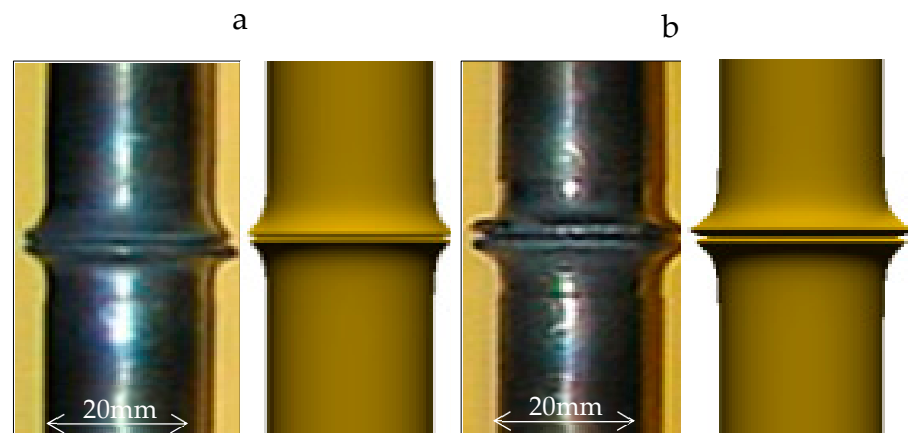


Figure 9. Comparison of the weld flash dimensions of SGCI friction welds with numerical simulation for the following parameters: FF = 29 kN, FT = 30 s, UF = 34 kN, UT = 3 s for specimen 1—(a), and FF = 24 kN, FT = 45 s, UF = 24 kN, and UT = 3 s for specimen 2—(b).

Figure 9 shows the nearly identical flash morphologies. A quantitative comparison of the flash dimensions obtained by experimental and numerical simulations is presented in Table 3. Axial shortening is also shown for comparison.

Table 3. Comparison of flash diameters and axial shortening.

	Flash Diameter 1, mm	Flash Diameter 2, mm	Shortening, mm
Measurement *	26.29	24.81	5.59
Predicted *	24.95	24.37	4.82
Measurement **	28.51	28.89	5.58
Predicted **	27.37	25.94	7.08

* (FF = 29 kN, FT = 30 s, UF = 34 kN, UT = 3 s), ** (FF = 24 kN, FT = 45 s, UF = 24 kN, UT = 3 s).

3.3.3. Critical ‘Damage’ Value

Figure 10 shows the post-processor ‘damage value’ and predicts the cracks on the flash weld. The Cockcroft and Latham damage model showed a superior prediction of ductile fracture [35]. Damage value ‘C’ is defined as the integrated area beneath the stress–strain curve up to the fracture [36].

$$\int_0^{\bar{\epsilon}_f} \frac{\dot{\sigma}}{\bar{\sigma}} d\bar{\epsilon} = C \quad (10)$$

where $\bar{\epsilon}_f$ is fracture strain, $\dot{\sigma}$ is maximum principal stress, $\bar{\sigma}$ is effective stress, $\bar{\epsilon}$ is effective strain, and C is the damage value.

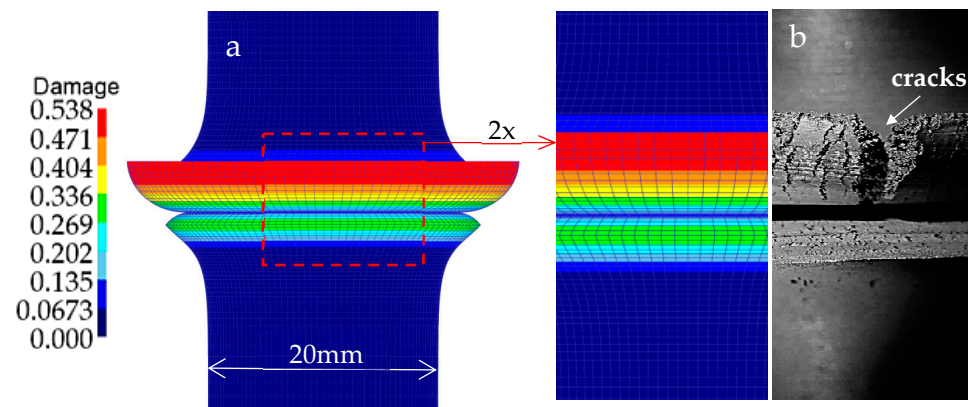


Figure 10. The post-processor damage value (a) predicted the cracks on the flash weld (b).

This ductile fracture criterion could be the best for real applications. The highest value of 0.538 was located in the weld flash (Figure 10a). The formation of ‘C’ values on the flash may suggest the possibility of cracks in this place. It was confirmed by observations in the flash weld (Figure 10b).

3.4. Effect of Friction Time on Temperature

Figure 11 shows distance and time curves for spheroidal graphite cast iron welds.

Figure 11 shows the distribution of temperature during the heating stage of the friction welding process. The temperature profiles correspond to times 1, 2, 4, 8, and 16 s. Symmetrical temperature curves occur across the interface (Figure 11). Temperature drops decay slowly in the spheroidal graphite cast iron. A large heat-affected zone occurs on the spheroidal graphite cast iron. Figure 11 indicates that, as the friction time increases, the temperature in the joint increases, reaching maximum values at the weld interface.

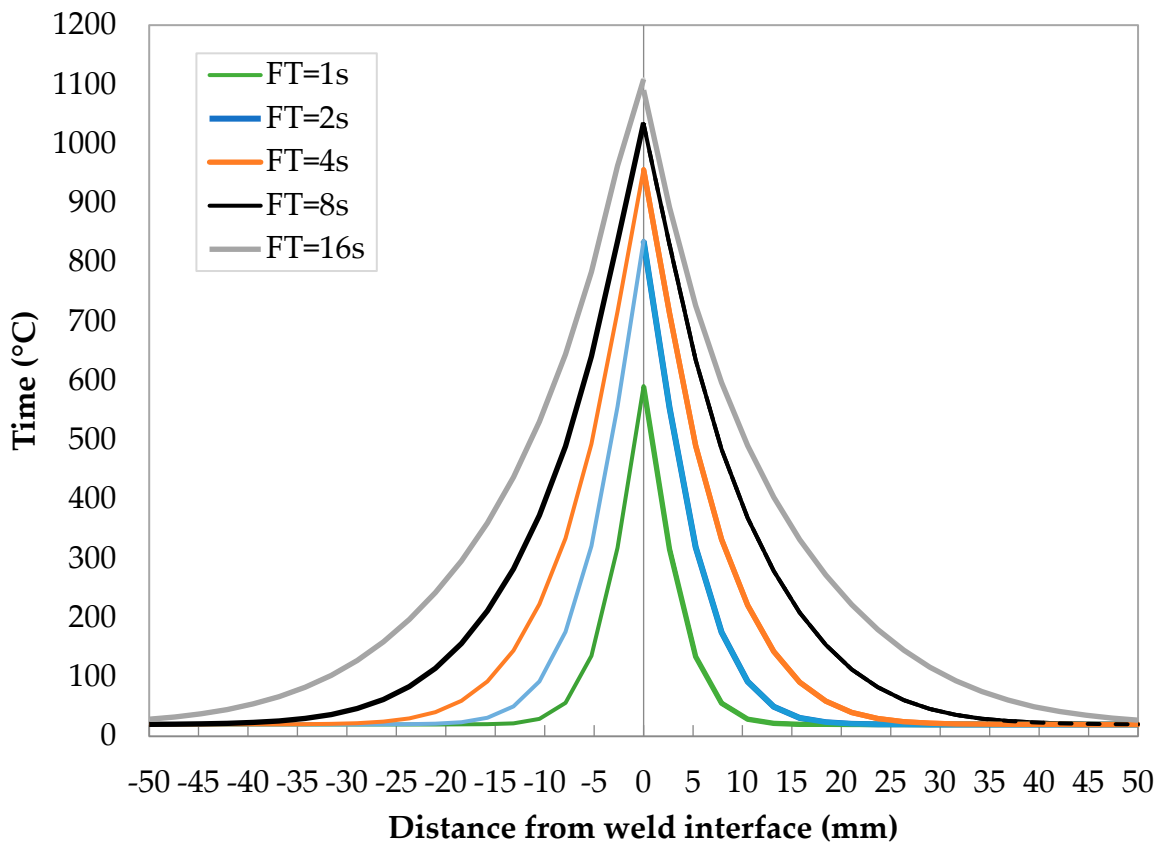


Figure 11. Axial centerline temperature, distance, and time curves for SGCI welds.

3.5. Influence of Friction Force on Axial Shortening

Figure 12 presents the influence of friction force on axial upsetting for friction forces of 18, 24, 33, and 37 kN.

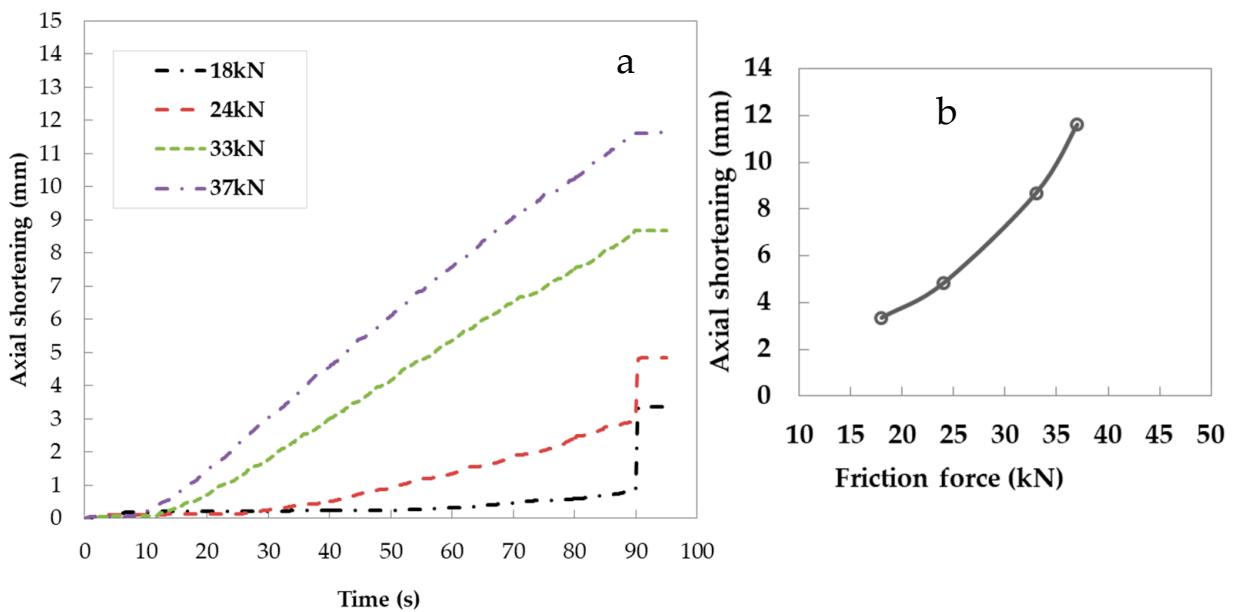


Figure 12. Effect of friction force on axial shortening: axial shortening vs. time (a) axial shortening vs. friction force (b).

During the friction stage between two materials, a small axial shortening occurs. As the friction time increases (from 18 to 37 kN), the axial shortening of the samples increases linearly. A logarithmic shortening of the material occurs during axial forces from 18 to 37 kN (Figure 12b). The maximum shortening of the material did not exceed 12 mm at the end of the friction phase. After this time, plastic deformation occurs, and a weld flash is produced. This process lasts a few seconds. A quick loss of material occurs after applying the upsetting force. The maximum material shortening was 12 mm for a friction force of 37 kN. Figure 12a shows that the forging period has minimal impact on the upset of the material. The axial shortening is practically unchanged in this stage [40].

4. Conclusions

The FE modelling of the nonlinear heat transfer problem at the interface of ductile cast iron bars during the friction process was successfully used in this study. The model was developed according to the characteristics of the friction welding process. The temperature, plastic deformations of weld, and stress distributions were calculated on friction welding SGCI workpieces. The predicted temperature profile of the friction welding is in fair agreement with the experimental investigation carried out. The highest value of 0.538 ‘damage’ is located in the flash, whereas cracking of the flash is observed. The predicted maximum temperatures in the axis, $1/2$ radius, and 2 mm from the surface of the sample amounted to 1162 °C, 1177 °C, and 1061 °C, respectively. The maximum temperature of the spheroidal graphite cast iron joint was below the melting temperature of the base material (~1350 °C). A quantitative comparison of the flash dimensions obtained by experiment and numerical simulations is nearly identical.

Author Contributions: Conceptualization and Methodology, R.W. and A.S.; Software, R.W.; Modelling, R.W.; Validation, R.W. and A.S.; Formal analysis, R.W.; Investigation, R.W. and A.S.; Resources, R.W.; Writing—original draft preparation, R.W.; Writing—review and editing, R.W.; Visualization, R.W.; Supervision, R.W. All authors have read and agreed to the published version of the manuscript.

Funding: This research received no external funding.

Data Availability Statement: Data are contained within the article.

Acknowledgments: The authors wish to thank Mieczysław Kaczorowski from the Faculty of Mechanics of Institute of Mechanics and Design, Warsaw University of Technology, for his valuable suggestions.

Conflicts of Interest: The authors declare no conflicts of interest.

References

- Guo, Z.; Ma, T.; Yang, X.; Li, J.; Li, W.; Vairis, A. Multi-scale analyses of phase transformation mechanisms and hardness in linear friction welded Ti17(α + β)/Ti17(β) dissimilar titanium alloy joint. *Chin. J. Aeronaut.* **2024**, *37*, 312–324. [[CrossRef](#)]
- Guo, Z.; Ma, T.; Yang, X.; Tao, J.; Li, W.; Li, J.; Vairis, A.A. In-situ investigation on dislocation slip concentrated fracture mechanism of linear friction welded dissimilar Ti17(α + β)/Ti17(β) titanium alloy joint. *Mater. Sci. Eng. A* **2023**, *872*, 144991. [[CrossRef](#)]
- American Welding Society. Specifications and standards. In *Recommended Practice for Friction Welding*; American Welding Society: Miami, FL, USA, 1989.
- Withers, P.J.; Preuss, M. *Simulation of Rotational Welding Operations*; Metals Process Simulation, ASM Handbook; ASM International: Detroit, MI, USA, 2010; Volume 22B.
- Vill, V.I. *Friction Welding of Metals*; AWS: New York, NY, USA, 1962.
- Cheng, C.J. Transient temperature distribution during friction welding of two similar materials in tubular form. *Weld J.* **1963**, *12*, 223–240.
- Rich, T.; Roberts, R. Thermal Analysis for Basic Friction Welding. *Met. Constr. Br. Weld. J.* **1971**, *3*, 93–98.
- Imshennik, K.P. Heating in Friction Welding. *Weld. Prod.* **1973**, *20*, 76–79.
- Healy, J.; McMullan, D.J.; Bahrani, A.S. Analysis of Frictional Phenomena in Friction Welding of Mild Steel. *Wear* **1976**, *37*, 279–289. [[CrossRef](#)]
- Kinley, W. Inertia Welding: Simple in Principle and Application. *Weld. Met. Fabr.* **1979**, *10*, 585–589.
- Murti, K.G.; Sundaresan, S. Parameter Optimization in Friction Welding Dissimilar Materials. *Met. Constr. Br. Weld. J.* **1983**, *15*, 331–335.
- Sahin, Z.; Yilbas, B.S.; Al-Garni, A.Z. Friction welding of Al–Al, Al–steel, and steel–steel samples. *J. Mater. Eng. Perform.* **1996**, *5*, 89–99. [[CrossRef](#)]

13. Służalec, A. Thermal Effects in Friction Welding. *Int. J. Mech. Sci.* **1990**, *32*, 467–478. [[CrossRef](#)]
14. Służalec, A. Solution of thermal problems in friction welding. *Int. J. Heat Mass Transf.* **1993**, *36*, 1583–1587. [[CrossRef](#)]
15. Bendzsak, G.J.; North, T.H.; Li, Z. Numerical Model for Steady-State Flow in Friction Welding. *Acta Mater.* **1997**, *45*, 1735–1745. [[CrossRef](#)]
16. Fu, L.; Duan, L. The Coupled Deformation and Heat Flow Analysis by Finite Element Method during Friction Welding. *Weld. Res. Suppl.* **1998**, *77*, 202–207.
17. Alvisé, L.D.; Massoni, E.; Walloe, S.J. Finite Element Modelling of the Inertia Friction Welding Process between Dissimilar Materials. *J. Mater. Process. Technol.* **2002**, *125*, 387–391.
18. Balasubramanian, V.; Li, Y.; Stotler, T.; Crompton, J.; Soboyejo, A.; Katsube, N.; Soboyejo, W.A. New Friction Law for the Modelling of Continuous Drive Friction Welding: Applications to 1045 Steel Welds. *Mater. Manuf. Process.* **1999**, *14*, 845–860. [[CrossRef](#)]
19. Maalekian, M.; Kozeschnik, E.; Brantner, H.P.; Cerjak, H. Comparative analysis of heat generation in friction welding of steel bars. *Acta Mater.* **2008**, *56*, 2843–2855. [[CrossRef](#)]
20. Pietras, A.; Papkala, H. The influence of friction conditions on thermal processes occurring in friction heating of dissimilar materials. *Weld. Res. Counc. Bull.* **1999**, *5*, 121–129. (In Polish)
21. Xiong, J.T.; Li, J.L.; Wei, Y.N.; Zhang, F.S.; Huang, W.D. An analytical model of steady-state continuous drive friction welding. *Acta Mater.* **2013**, *61*, 1662–1675. [[CrossRef](#)]
22. Hazman, S.; Ahmad, M.I.; Endri, R.; Zainal, A.H. Mechanical evaluation and thermal modeling of friction welding of mild steel and aluminium. *J. Mater. Process. Technol.* **2010**, *210*, 1209–1216.
23. Zimmerman, J.; Włosiński, W.; Lindemann, Z.R. Thermo-mechanical and diffusion modelling in the process of ceramic-metal friction welding. *J. Mater. Process. Technol.* **2009**, *209*, 1644–1653. [[CrossRef](#)]
24. Winiczenko, R.; Kaczorowski, M.; Skibicki, A. The microstructures, mechanical properties, and temperature distributions in nodular cast iron friction-welded joint. *J. Braz. Soc. Mech. Sci. Eng.* **2018**, *40*, 347. [[CrossRef](#)]
25. Winiczenko, R. Effect of friction welding parameters on the tensile strength and microstructural properties of dissimilar AISI 1020-ASTM A536 joints. *Int. J. Adv. Manuf. Technol.* **2016**, *84*, 941–955. [[CrossRef](#)]
26. Winiczenko, R.; Skibicki, A.; Skoczylas, P.; Trajer, J. Multi-objective optimization of the process parameters for friction welding of dissimilar metals. *E3S Web. Conf.* **2019**, *132*, 01028. [[CrossRef](#)]
27. Raghav, A.K.; Vaira Vignesh, R.; Kalyan, K.P.; Govindaraju, M. Friction welding of cast iron and phosphor bronze. *J. Inst. Eng. India Ser. C* **2020**, *101*, 347–354. [[CrossRef](#)]
28. Kimura, M.; Yoneda, A.; Kusaka, M.; Kaizu, K.; Hayashida, K.; Takahashi, T. Weldability and its improvement of friction welded joint between ductile cast iron and 5052 al alloy. *J. Adv. Mech. Des. Syst. Manuf.* **2021**, *15*, JAMDSM0045. [[CrossRef](#)]
29. Trupiano, S.; Belardi, V.G.; Fanelli, P.; Gaetani, L.; Vivio, F. A novel modeling approach for multi-passes butt-welded plates. *J. Therm. Stress.* **2021**, *44*, 829–849. [[CrossRef](#)]
30. Baruah, S.; Singh, I.V. A framework based on nonlinear FE simulations and artificial neural networks for estimating the thermal profile in arc welding. *Finite Elem. Anal. Des.* **2023**, *226*, 104024. [[CrossRef](#)]
31. Aberbache, H.; Corolleur, A.; Mathieu, A.; Laurent, F.; Bolot, R.; Bleurvacq, L. Experimental analysis and numerical simulation of laser welding of thin austenitic stainless-steel sheets using two models: Bilinear isotropic strain hardening model and Johnson–Cook model. *J. Adv. Join. Process.* **2024**, *9*, 100198. [[CrossRef](#)]
32. Winiczenko, R.; Skibicki, A.; Skoczylas, P. The Experimental and FEM Studies of Friction Welding Process of Tungsten Heavy Alloy with Aluminium Alloy. *Appl. Sci.* **2024**, *14*, 2038. [[CrossRef](#)]
33. Kobayashi, S.; Oh, S.; Alan, T. *Metal Forming and Finite Element Method*; Oxford University Press: New York, NY, USA, 1989.
34. Singh, S.K.; Chattopadhyay, K.; Phanikumar, G.; Dutta, P. Experimental and numerical studies on friction welding of thixocast A356 aluminum alloy. *Acta Mater.* **2014**, *73*, 177–185. [[CrossRef](#)]
35. Li, W.; Wang, F. Modeling of continuous drive friction welding of mild steel. *Mater. Sci. Eng. A* **2011**, *528*, 5921–5926. [[CrossRef](#)]
36. Nu, H.; Le, T.; Minh, L.; Loc, N. A Study on Rotary Friction Welding of Titanium Alloy (Ti6Al4V). *Adv. Mater. Sci. Eng.* **2019**, *2019*, 4728213.
37. Wang, F.F.; Li, W.Y.; Li, J.L.; Vairis, A. Process parameter analysis of inertia friction welding nickel-based superalloy. *Int. J. Adv. Manuf. Technol.* **2014**, *71*, 1909–1918. [[CrossRef](#)]
38. Geng, P.; Qin, G.; Zhou, J. Numerical and experimental investigation on friction welding of austenite stainless steel and middle carbon steel. *J. Manuf. Process.* **2019**, *47*, 83–97. [[CrossRef](#)]
39. Heppner, E.; Woschke, E. A framework for modelling the manufacturing process of friction welded lightweight structures. *Finite Elem. Anal. Des.* **2022**, *205*, 103751. [[CrossRef](#)]
40. Zang, Q.Z.; Zhang, L.W.; Liu, W.W.; Zhang, V.G.; Qu, S. 3D rigid viscoplastic FE modelling of continuous drive friction welding process. *Sci. Technol. Weld. Join.* **2006**, *11*, 737–743. [[CrossRef](#)]
41. Lei, B.; Shi, Q.; Yang, L.; Liu, C.; Pan, J.; Chen, G. Evolution of interfacial contact during low pressure rotary friction welding: A finite element analysis. *J. Manuf. Process.* **2020**, *56*, 643–655. [[CrossRef](#)]
42. Jin, F.; Li, J.; Liu, P.; Nan, X.; Li, X.; Xiong, J.; Zhang, F. Friction coefficient model and joint formation in rotary friction welding. *J. Manuf. Process.* **2019**, *46*, 286–297. [[CrossRef](#)]

43. Jin, F.; Li, J.; Du, Y.; Nan, X.; Shi, J.; Xiong, J.; Zhang, F. Numerical simulation based upon friction coefficient model on thermo-mechanical coupling in rotary friction welding corresponding with corona-bond evolution. *J. Manuf. Process.* **2019**, *45*, 595–602. [[CrossRef](#)]
44. Tang, T.; Shi, Q.; Lei, B.; Zhou, J.; Gao, Y.; Li, Y.; Zhang, G.; Chen, G. Transition of interfacial friction regime and its influence on thermal responses in rotary friction welding of SUS304 stainless steel: A fully coupled transient thermomechanical analysis. *J. Manuf. Process.* **2022**, *82*, 403–414. [[CrossRef](#)]
45. Jin, F.; Shi, J.; Wen, G.; Fu, B.; Shen, J.; Wang, S.; Wu, J.; Xiong, J.; Li, J. Frictional heat induced morphological responses at the interface in rotary friction welding of austenitic alloys: Corona-bond and heat-pattern. *J. Mater. Res. Technol.* **2023**, *23*, 5972–5992. [[CrossRef](#)]
46. Xu, Y.; Chen, W.; Li, W.; Yang, X. Numerical simulation of rotary friction welding of Ti-6Al-4V tubes. *Weld. World.* **2023**, *67*, 2671–2681. [[CrossRef](#)]
47. Li, W.; Shi, S.; Wang, F.; Zhang, Z.; Ma, T.; Li, J. Numerical Simulation of Friction Welding Processes Based on ABAQUS Environment. *J. Eng. Sci. Technol. Rev.* **2012**, *5*, 10–19. [[CrossRef](#)]
48. Sobolev, A.V.; Radchenko, M.V. Use of Johnson–Cook plasticity model for numerical simulations of the SNF shipping cask drop tests. *Nucl. Technol.* **2016**, *2*, 272–276. [[CrossRef](#)]
49. Perovic, N.L.; Maglic, K.D.; Stanimirovic, A.M.; Vukovic, G.S. Transport and calorimetric properties of AISI 321 by pulse thermal diffusivity and calorimetric techniques. *High Temp. High Press.* **1995**, *1*, 53–58. [[CrossRef](#)]

Disclaimer/Publisher’s Note: The statements, opinions and data contained in all publications are solely those of the individual author(s) and contributor(s) and not of MDPI and/or the editor(s). MDPI and/or the editor(s) disclaim responsibility for any injury to people or property resulting from any ideas, methods, instructions or products referred to in the content.